



Original Article

Liquid metal infiltration of silicon based alloys into porous carbonaceous materials. Part II: Experimental verification of modelling approaches by infiltration of Si-Zr alloy into idealized microchannels

Manoj Naikade^{a,b,*}, Caroline Hain^a, Kaja Kastelik^a, Rolf Brönnimann^a, Giovanni Bianchi^c, Alberto Ortona^c, Thomas Graule^a, Ludger Weber^b

^a Empa – Swiss Federal Laboratories for Materials Science and Technology, Dübendorf, Switzerland

^b Laboratory of Mechanical Metallurgy, Ecole Polytechnique Fédérale de Lausanne, EPFL, Lausanne, Switzerland

^c Scuola universitaria professionale della Svizzera italiana, Lugano, Switzerland

ARTICLE INFO

Keywords:

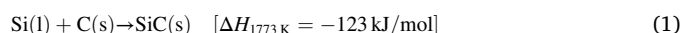
LSI
RMI
SiC composites
Si-Zr alloy infiltration
Microchannel

ABSTRACT

In this work, the mechanisms leading to the pore closure in reactive melt infiltration (RMI) of carbon by pure silicon and a near eutectic Si-8 at-pct Zr alloy at 1500 and 1700 °C under vacuum were studied. Various geometrical configurations of microchannels were fabricated via laser ablation of glassy carbon plates. The micron size capillary channels allowed simplifying the complicated porosity distribution in the infiltration of powder or fibres based porous preform while keeping the physical dimensions in the range of where the physical phenomenon of pore closure takes place. The extent of infiltration was analysed by means of X-ray radiography. For RMI of pure Si, the widely accepted decrease in capillary radius by the formation of a solid state SiC layer by the reaction of liquid Si and C was observed, but did not lead to closure and it is hence not the infiltration limiting step in channels as small as 10 µm. However, in the case of the Si-Zr alloy infiltration, another mechanism of pore closure was observed, namely the precipitation of zirconium silicides at the infiltration front, due to Zr enrichment in the alloy by the continuous consumption of Si for the formation of SiC.

1. Introduction

Silicon infiltrated silicon carbide (Si-SiC), first developed by Popper in 1960s [1], has gained popularity as an industrial ceramic material, known for its remarkable properties, such as low porosity, low density, high thermal conductivity, high mechanical strength, excellent chemical, oxidation and thermal shock resistance and high wear and corrosion resistance [2,3]. Increasing interest led to the development of many variants, such as monolithic and particle or fibre reinforced ceramic matrix composites (CMC). Although they can be obtained from different constituents and processes [4–7], the fabrication concept is based on the reactive melt infiltration (RMI) process, also known as liquid silicon infiltration (LSI) in the case of Si infiltration. The general idea consists of infiltrating a porous carbonaceous preform by liquid Si to attain a fully dense Si-SiC composite. The liquid Si is pulled into the porous preform, driven by capillary forces where a chemical reaction occurs between the liquid Si and solid C, resulting in a solid SiC matrix, according to the following reaction [8]:



where *l* is liquid, *s* is solid and ΔH is enthalpy of formation.

This reaction is highly exothermic, potentially causing an increase in local temperature by several hundred degrees. This, in turn, results in the occurrence of thermal stresses within the material, which could potentially lead to material failure [9,10]. Additionally, depending on the pore characteristics and the reactivity of the preform, capillary blockage and, as a consequence, incomplete infiltration may take place [11]. The diffusion of C through solid SiC is faster than that of Si; therefore, the growth of solid state reaction product proceeds also into the pore space, potentially blocking further transport of liquid Si [12–14]. Moreover, the remaining unreacted Si expands during solidification, inducing additional stress concentrations [15]. Various approaches have been made to overcome these issues, such as including inert interphase such as SiC or BN, by chemical vapour deposition (CVD) of carbon fibres followed by infiltration. These techniques, however, being effective, remain expensive in terms of processing and equipment.

* Corresponding author at: Empa – Swiss Federal Laboratories for Materials Science and Technology, Dübendorf, Switzerland.

E-mail address: manojknaikade@gmail.com (M. Naikade).

<https://doi.org/10.1016/j.jeurceramsoc.2022.01.004>

Received 6 September 2021; Received in revised form 31 December 2021; Accepted 3 January 2022

Available online 5 January 2022

0955-2219/© 2022 The Author(s). Published by Elsevier Ltd. This is an open access article under the CC BY license (<http://creativecommons.org/licenses/by/4.0/>).

Furthermore, they hamper the conversion reaction and, hence, do not solve the problem of limited operation temperature, restricted by residual Si. An alternative approach is to use metal – silicon alloys, as they not only lower the amount of residual Si by the formation of high temperature silicides but also lower the infiltration temperature [16–19]. The alloying element is selected based on liquid-phase equilibria and the ability to form refractory silicides with higher melting temperatures than pure Si. This has been demonstrated using Si-Mo, Si-Zr, Si-Co and Si-Hf alloys [20–27]. Alloying elements that tend to form carbides, such as Al, are undesirable since they do not help to address the underlying issue of unreacted Si, and the carbides degrade the composite's mechanical properties [28,29]. Several researchers have also studied the wetting behaviour of Si and Si alloys on various types of graphite and SiC [9,30–38], increasing the understanding of the physical principles behind Si and metal – Si alloys infiltration. However, certain phenomena occurring at the micron scale remain unclear. Classical sessile drop experiments [34,39], millimetre sized capillaries [40] or direct observations of preform infiltration [41–43] are commonly used to characterize the reactive infiltration process; however, the differences in experimental macroscopic scale may overlook certain effects, which could only be observed at the micron scale.

In particular the phenomenon of blockage of the infiltration capillary at the entrance of the capillary system by excessive formation of the reaction products is absent in scaled experimental setups. Besides the blockage by carbide formation at the entrance it can also be conceived that blockage will happen by enrichment of the alloying elements at the infiltration front. The first part of the series of papers has laid the mathematical framework to estimate under which conditions either type of blockage will be observable. In this second part we present results of infiltration experiments with idealized geometries that allow to confront the predictions made in part I [47] with experiment.

In this study, the process of Si-SiC composite formation by RMI was idealized by infiltration experiments of carbon capillary microchannels with pure Si and near eutectic Si-8 at-pct Zr alloy at 1500 and 1700 °C. By infiltrating microchannels of various designs, produced using laser ablation, it was possible to simplify the complicated porosity distribution in porous preforms while maintaining the physical dimensions in the range at which the physical phenomenon of pore closure takes place. The experimental products were analysed using X-ray radiography and scanning electron microscopy (SEM), the characterization of which allows further enhancing our understanding of the capillary closure phenomenon during RMI of Si and Si-Zr alloy.

2. Materials and methods

2.1. Material

Vitreous carbon plates (SIGRADUR-G, HTW, Germany), also referred to as glassy carbon, were selected as the source of carbon due to their dense structure compared to graphite plates, which tend to have significant porosity. For RMI, pure Si (Sicorma GmbH, Germany) and near eutectic Si-8 at-pct Zr alloy (Chengdu Huarui Industrial Co Ltd., China) were used.

2.2. Fabrication of microchannels

Microchannels, with a depth ranging from 0.01 to 0.1 mm and length of up to 460 mm, were fabricated using laser ablation. For machining the channels, a pulsed laser (SuperRapid laser from Lumera GmbH) was used. The short pulse laser operates at a wavelength of 355 nm (frequency tripled) and has a nominal pulse length of 10 ps. The laser pulses were directed towards the sample via a galvano scan head (ScanLab GmbH). For ablation, a pulse repetition rate of 160 kHz and pulse energy of about 14 µJ (2.2 W average power) was used. The structure was written with a hatched pattern. A total of six hatch directions (0°, 90°, 30°, 120°, 60°, 150°) were applied to achieve a smooth surface. The

required depth was achieved by adjusting the pulse energy and the number of repetitions. Since the pattern was larger than the writing area of the scan head stitching was applied. A graded transition zone was used to minimize edges between the stitching areas.

Various configurations of channels were produced to study different aspects of reactive infiltration, summarized in Table 1 and depicted in Fig. 1.

2.3. Infiltration setup

Two vitreous carbon plates, one flat and unmachined and one with laser ablated microchannels were clamped together using graphite clamps and bolts sourced from Steinemann Carbon AG, Switzerland (2 clamps for 50 mm-long and 3 for 100 mm-long samples), as schematically shown in Fig. 2. The carbon plates were cleaned in an ultrasonic bath for 5 min in isopropyl alcohol and then dried using a clean compressed gas canister (Druckluft 67, Kontakt Chemie, Belgium) just before clamping them together. Utmost care was taken to avoid any dust entrapment in the channels. In this way, we were able to achieve the effective capillary sizes as low as 10 µm and the maximum available infiltration length up to 465 mm as compared to the 250 µm radii and the maximum length of infiltration of 7 mm in the work of Sergi et al. [40].

Approximately 80 g of pure silicon or the eutectic Si-8 at-pct Zr alloy was placed in a crucible made up of graphite foil (SGL, Germany) coated with a boron nitride spray (3M, Germany). The graphite foil crucible was next placed into a larger graphite crucible. The clamped infiltration form was situated slightly above the bottom of the graphite foil crucible by two graphite rods, as shown in Fig. 3. Finally, the whole setup was put in a graphite heated vacuum furnace (FCT, Germany). The furnace was heated to 1500 or 1700 °C at the rate of 300 °C/h under a vacuum of $\sim 5 \times 10^{-2}$ mbar. After reaching the final temperature, the heating was turned off and the furnace was let cool down.

2.4. Analyses

The surface roughness after polishing and after laser ablation was measured using a Leica DCM8 confocal microscope. The infiltrated microchannel samples were imaged via X-ray radiography using an RX solution EasyTom XL, France. The infiltrated fragment of the microchannels typically shows up darker than the rest of the carbon plate and empty channel. Based on the radiographs, the samples were cut using a diamond saw to observe infiltration cross-sections selectively. The samples were then mounted in resin and polished using an automatic polishing machine (TEGRAMIN, Struers GmbH, Switzerland) and 15, 9, 6 and 1 µm diamond suspensions and including a final polishing step

Table 1
Summary of dimensions of microchannels in various configurations.

Configuration	Channel number	Shape	Width (mm)	Depth (mm)	Length ^a (mm)
A	1	Straight	1	0.1	50
	2	Straight	4	0.1	50
	3	Straight	1	0.025	50
	4	Straight	4	0.025	50
B	1	Straight	1	0.1	100
	2	Straight	4	0.1	100
	3	Straight	1	0.025	100
	4	Straight	4	0.025	100
C	1	Straight	1	0.03/ 0.02/ 0.01	100/3
	2	Rectangular bend	1	0.02	241
	3	Curved bend	1	0.02	207
D	1	Curved bend	1	0.01	465

^a Along the centre-line of the channel.

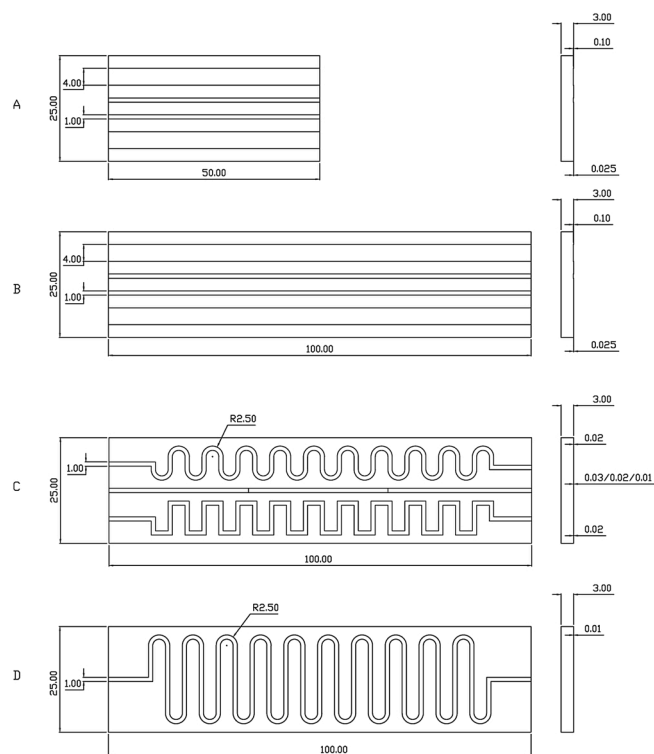


Fig. 1. Various configurations of microchannels with their dimensions used in this research. Length indications are in mm.

with 0.5 μm alumina suspension. The reaction layer and interphase were analysed using a scanning electron microscope and EDX (Tescan VEAG3 with Bruker AXS Quantax 200 EDX system).

3. Results and discussion

3.1. Surface roughness

The surface roughness values determined using confocal microscopy by Leica DCM8 microscope in accordance with ISO 4287 for R_a and ISO 25178 for S_a values are summarized in Table 2.

3.2. Microchannel characterization

3.2.1. Configuration A

Microchannel configuration A was designed to study the effect of the aspect ratio of the channels and the effect of side edges. Pure Si was used to infiltrate the microchannels at 1500 $^{\circ}\text{C}$. The X-ray radiograph taken after the infiltration showed complete infiltration of all 4 channels (Fig. 4). In the X-ray radiograph, the channels filled with Si appears darker than the unfilled channels. The four microchannels had width-to-depth aspect ratios varying from 10 to 160, as shown in Table 3.

SEM analysis of each Si infiltrated microchannel was carried out at the height of 15, 25 and 35 mm from the bottom. Multiple images from each microchannel were combined to measure the average thickness of the reaction layer. For this purpose, the grid was put onto every image to ensure equal distances between the consecutive measurements. In Fig. 5 (a), an example of an SEM image made by the panoramic stitching of several high resolution pictures from the cross section of the 1 mm by 0.1 mm microchannel is shown with the typical grid used to measure the reaction layer thickness at a fixed interval. The black part in the image is carbon, and the light part is the channel filled with solidified Si. The darker gray phase at the microchannel walls is the SiC reaction layer. The measurements of reaction layer thickness were carried out every 25 μm . Afterward, they were divided into three groups, namely the left edge, middle and right edge, to investigate the potential effect of the edges on the formation of the reactive layer. Moreover, the opposite walls of the channels were analyzed separately since the reactivity of the polished and the laser ablated surface might be different. Henceforth, the designation 'bottom' refers to the microchannel wall influenced by the laser ablation process, whereas 'top' is the opposite, not influenced, as-polished surface. In Fig. 5(b), the average thickness of the reaction layer of four microchannels with aspect ratios from 10 to 160 are plotted for three groups left edge (L), middle (M) and right edge (R). The systematic layer thickness measurement did not show any trend from the left edge to the right edge. Also, the thickness of the reaction layer did not show any significant change along the length of infiltration. Therefore, the assumption of two infinite parallel plates separated by a micron size gap forming a microchannel along the length can be considered valid. However, a significant difference in reaction layer thickness was found between each channel's top and bottom walls. One possible reason behind this behaviour is a strong correlation between surface roughness and reactivity as has been observed by others previously [44,45].

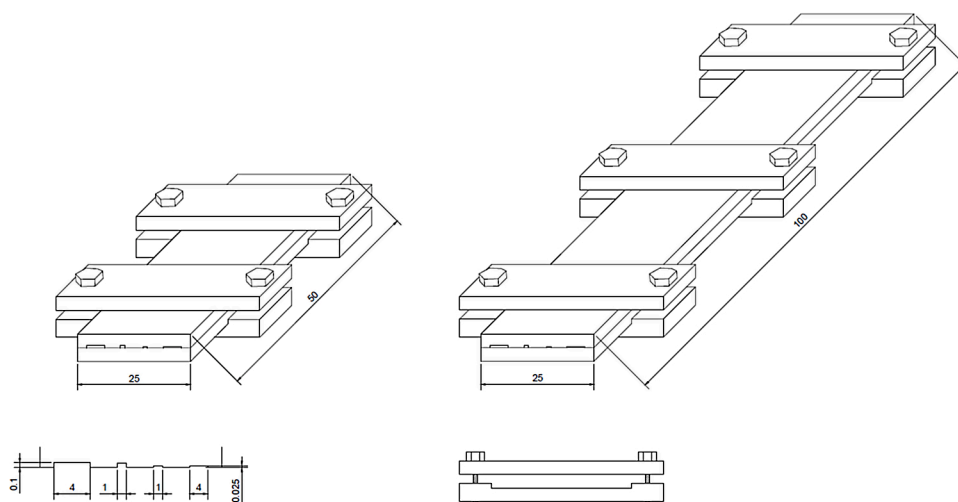


Fig. 2. Schematic of capillary microchannel assembly by clamping vitreous carbon plate with laser ablated groove together with another vitreous carbon plate. Length indications are in mm.

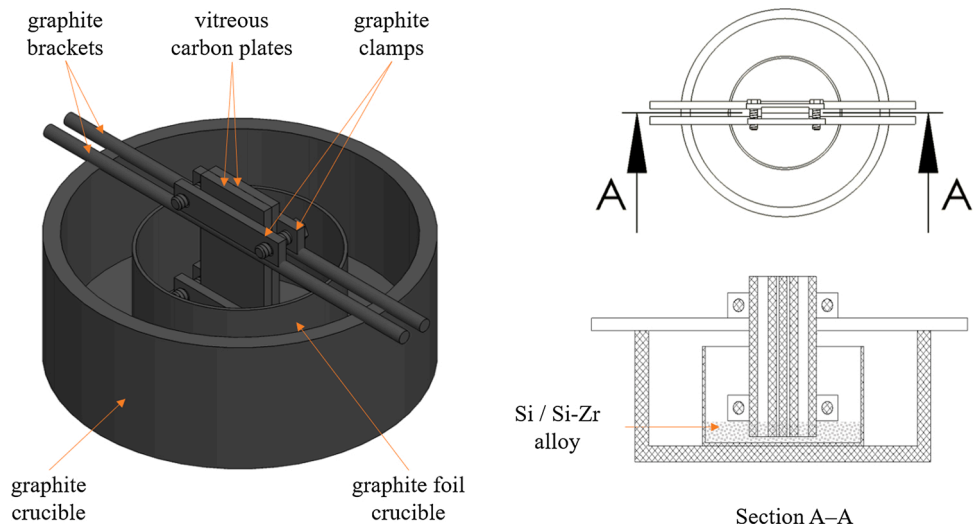


Fig. 3. Experimental setup of infiltration showing microchannel made by clamping vitreous carbon plates being kept upright by graphite brackets in the graphite crucible. The melting Si or Si-Zr alloy was kept in the BN coated graphite foil crucible in the centre.

Table 2
Surface roughness of the polished surface and laser ablated surface of glassy carbon plate (measured on 20 μ m deep channel) measured by Leica DCM8.

Surface	R_a (nm)	S_a (nm)
As polished	3.4 ± 0.2	5.4 ± 0.6
Laser ablated	49.3 ± 2.5	185.0 ± 21

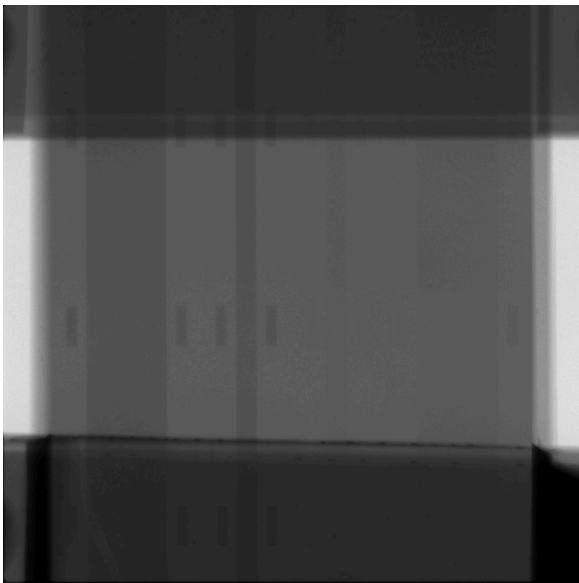


Fig. 4. Radiograph of microchannels in configuration A showing complete infiltration of all the channels.

Table 3
Aspect ratio of laser ablated microchannels in vitreous carbon.

Width (mm)	Depth (mm)	Aspect ratio
1	0.1	10
4	0.1	40
1	0.025	40
4	0.025	160

3.2.2. Configuration B

The dimensions of microchannels in configuration B was similar to configuration A except that the length was 100 mm instead of 50 mm. The small grooves, as seen in the radiograph (Fig. 6) were markers to observe the direction of formation of the reaction layers by measuring the distance between the outer edge of the microchannel and the marker. The sealing between the two plates was, however, insufficient to allow for this kind of observation since the alloy seeped through the tiniest gaps possible to fill the gaps. The microchannels were infiltrated by near eutectic Si-8 at-pct Zr alloy at 1500 °C. The radiograph showed complete infiltration along the whole length (Fig. 6). It can be seen from the radiograph that the zirconium-rich phase from the eutectic alloy is increasing as the infiltration proceeds. As the infiltration by alloy proceeds, the Si concentration of the alloy decreases due to reaction with carbon to form SiC. The reaction layer, in this case, was also found to be mainly SiC with some traces of trapped Zr as observed with SEM (Fig. 7). The SEM images of the 0.02 \times 1 microchannel taken at 0, 20, 40, and 60 mm (Fig. 7) from the microchannel entrance shows the correlation between the increase in the concentration of ZrSi₂ phase and the infiltration length to the corresponding region of the radiograph in Fig. 6.

3.2.3. Configuration C

Configuration C was designed to study the effect of tortuosity and change in the capillary thickness. The microchannel with rectangular bends would provide a more tortuous path with abruptly reducing velocity than the one with semi-circular bends. Both the channels had a depth of 0.02 mm, while the middle channel was straight and was divided into three equal parts with thickness 0.03 mm near the entrance, 0.02 mm in the centre part and 0.01 mm towards the end of the channel. The tortuous shape was also a means to increase the possible infiltration length of the channel.

The radiograph (Fig. 8(a)) shows that all three microchannels were completely infiltrated by Si-8 at-pct Zr alloy at 1500 °C. Some coarse Zr-rich primary phases can be seen in both the rectangular bend and the curved bend channels. As can be seen in the close-up image to the right, the Zr-rich phase is also present further in the direction of the infiltration front. It simply gets more finely dispersed. This can be interpreted as facilitated nucleation of the Zr-rich phase by larger oversaturation of zirconium, i.e., higher Zr-content. In the middle straight channel, the initial two sections with 0.03 and 0.02 mm depth had a fine eutectic structure. The top one-third section of approximately 33 mm with 0.01 mm depth showed a longer needle-like structure of Zr rich phase, which was extracted for phase fraction analysis using the grayscale

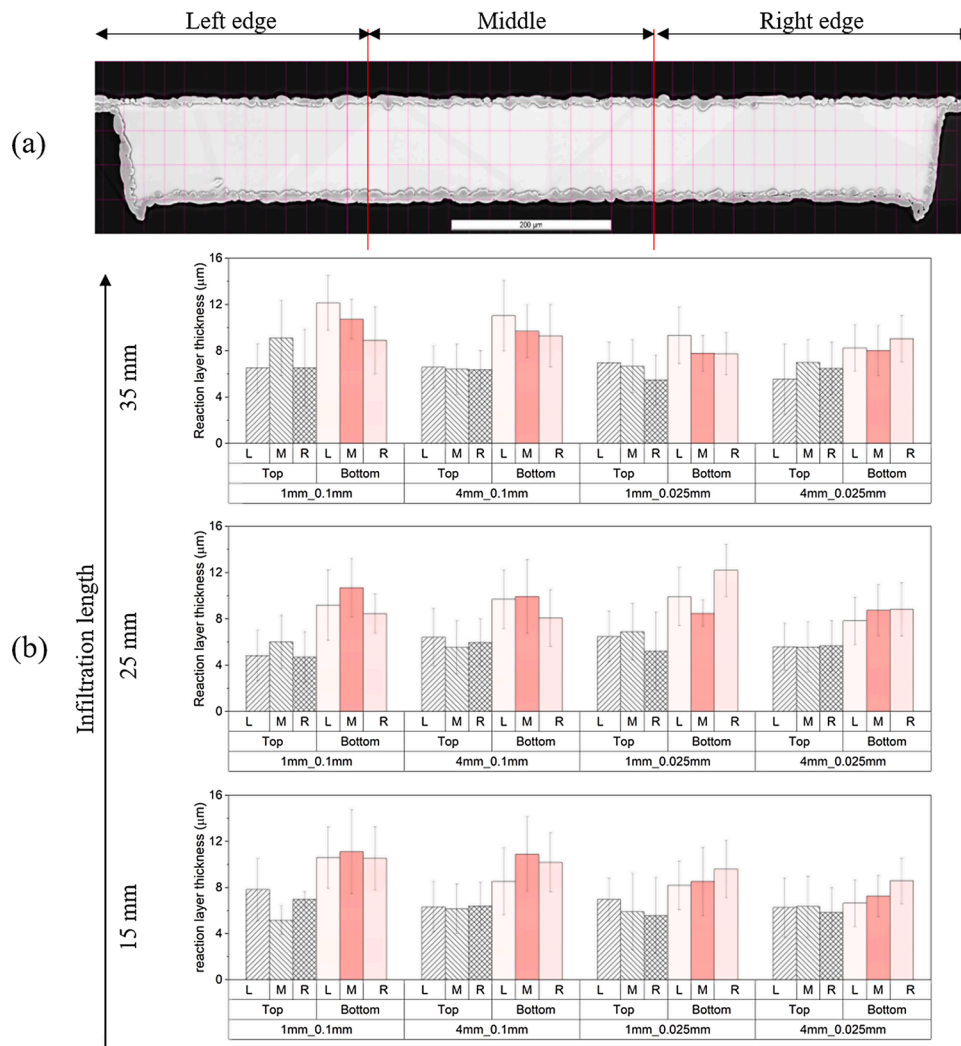


Fig. 5. (a) SEM image showing a cross-section of 1 mm by 0.1 mm microchannel infiltrated at 1500 °C in the sample with a grid for reaction layer's thickness measurements. (b) Reaction layer thickness along the infiltration length at 15, 25 and 35 mm from the bottom for all 4 channels divided into the left edge (L), middle (M) and right edge (R) and top and bottom laser ablated plate infiltrated by pure Si.

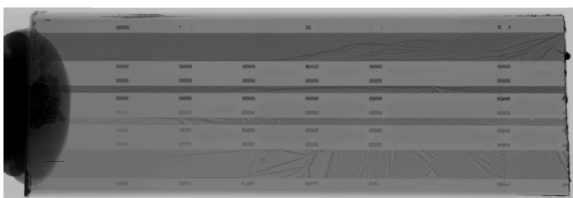


Fig. 6. Radiograph of microchannels of configuration B after infiltration by near eutectic Si-8 at-pct Zr alloy.

thresholding technique (Fig. 8(b)). The grayscale threshold was adjusted manually to separate Zr rich dark grey regions (presumably the ZrSi_2 primary phase) using the grayscale threshold function of Fiji [46] software. The fraction of the black region was then plotted against the length of infiltration. The tendency of a slight increase in Zr rich phase fraction can be observed; however, there was still complete infiltration of the microchannel.

3.2.4. Configuration D

The configuration D was designed with semi-circular bends to observe the effect of tortuosity in microchannels with a depth of 0.01 mm. The microchannel had a total length of 465 mm. The sample

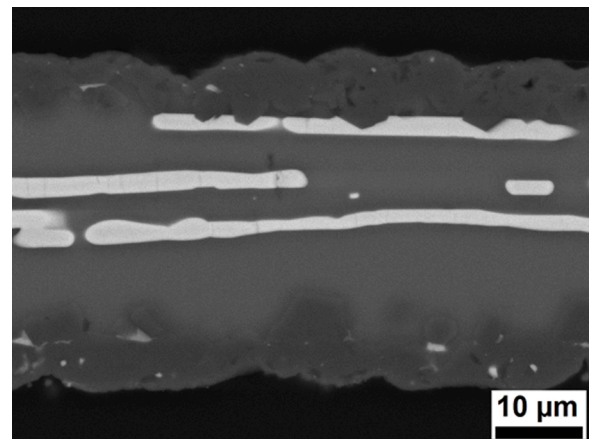


Fig. 7. SEM image of cross section of 1 mm × 0.025 mm microchannel at 20 mm from the bottom. The lighter part in the middle is Zr rich phase while the reaction layer is mainly SiC with some trapped Zr.

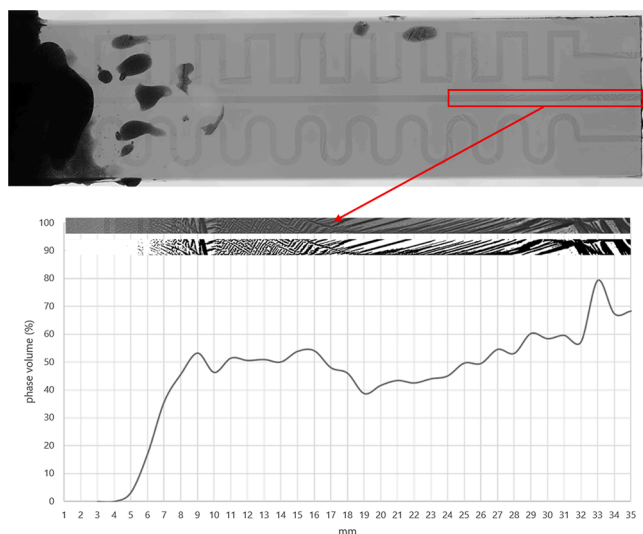


Fig. 8. (a) Radiograph of microchannels of configuration - C after infiltration by near eutectic Si-8 at-pct Zr alloy. (b) Phase fraction analysis of 0.01 mm section of the gradient channel. The black fraction represents the Zr-rich phase.

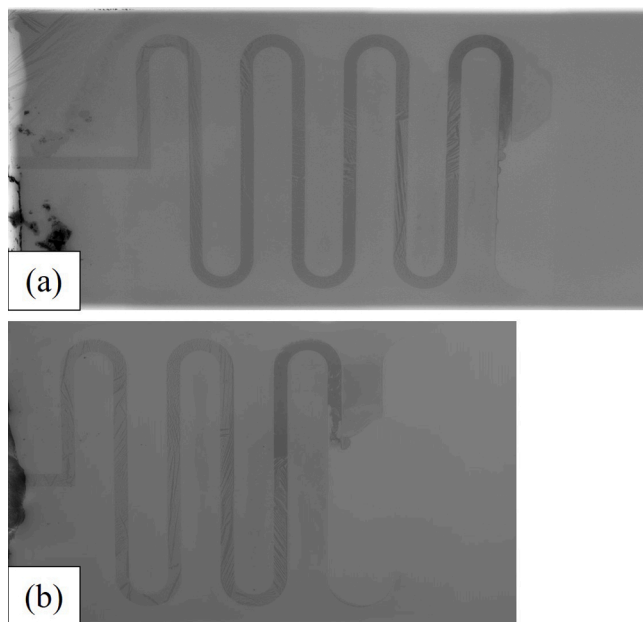


Fig. 9. Radiographs of two samples D1 and D2 after infiltration by Si-8 at-pct Zr alloy at 1500 °C.

D1 and D2 were infiltrated using Si-8 at-pct Zr alloy at 1500 °C. In Fig. 9, the so-called pore closure phenomenon was observed, where the infiltration of alloy stopped in the microchannel approximately at 166 and 120 mm from the entrance in sample D1 and D2, respectively. A similar effect of the increase in Zr-rich phase fraction along the length of

microchannel was observed. The radiograph of sample D3 after infiltration by pure Si at 1500 °C showed complete infiltration (Fig. 10). As the microchannels are very thin compared to the total thickness of 6 mm glassy carbon plate assembly, the contrast obtained in the radiograph due to the small difference in attenuation of SiC/Si in the microchannel compared to the glassy carbon plate is much lower than for the Si-Zr alloy. The results show that the infiltration of pure Si is dominated by triple line velocity and not affected by reduction in channel cross section due to the formation of the SiC layer even at 0.01 mm microchannels. In contrast, during the infiltration of Si-8 at-pct Zr alloy, the concentration of Si at the infiltration front keeps decreasing as infiltration proceeds along the microchannel due to the reaction of Si from liquid alloy with C from glassy carbon plate to form solid SiC layer at the interface. The enrichment of the infiltration front in Zr results in precipitation of Zr silicides, possibly causing the (intermittent) closure of the microchannel at the front.

The sample D4 was infiltrated by Si-8 at-pct Zr alloy at 1700 °C. In the radiograph (Fig. 11) after infiltration, the microchannel closure was observed at 322 mm. The higher infiltration temperature retards the precipitation of primary Zr-rich solid phases to higher Zr-concentrations.

3.3. The morphology of reaction layer between silicon and vitreous carbon

Several authors have carried out experimental studies on the reaction mechanism occurring at the Si/vitreous carbon interface [30,32,37, 47]. A general finding described the reaction formed layer as a bi-layer. We also observed a similar bi-layer in our experiments with both pure Si and Si-Zr alloy infiltrated microchannels, as seen in Fig. 5(a) and 7. The bi-layer can be clearly distinguished and observed in the BSE image (Fig. 12) of the cross section of 0.1 mm deep microchannel from configuration A. Initially, the layer I is formed at the interface by carbon dissolution followed by micron-sized SiC grain precipitation. The SiC particles of layer I subsequently dissolve and re-precipitate as faceted crystals forming layer II. The results, being in line with the research of Voytovych et al. [37] and Deike and Schwerdtfeger [47], lead to the general picture that this complex zone consists of a thin, continuous SiC layer (I), approximately 1–2 μm thick, separating so-called ‘pockets’ (I') from layer II. In layer II two different types of grains can be observed – faceted SiC crystals (denoted as IIa) and columnar SiC crystals (denoted as IIb). The single crystals can reach far into the Si. Some of them seems to be detached from the layer and being completely surrounded by the Si phase.

Despite the fact that the reaction layer thickness was observed to be nearly constant with increasing infiltration distance in the sample of configuration A, the morphology of SiC changes substantially, as shown in Fig. 13. These observations seem to be in agreement with the findings of Voytovych et al. [37] and Deike et al. [47]. They reported that for a long-term experiment, at times t longer than a certain critical time t^* , homogenization of the reaction zone occurs due to grain coarsening which then leads to disappearance of layer I.

The EDX point analysis across the reaction formed SiC layer at the interface between molten silicon, and the vitreous carbon microchannel of configuration A illustrates the changes in concentration of silicon as

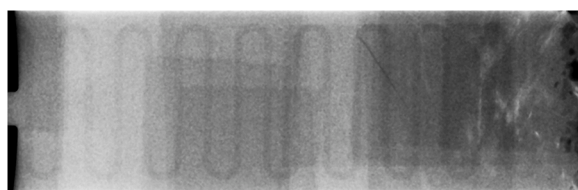


Fig. 10. Radiograph of sample D3 showing complete infiltration by pure Si at 1500 °C.

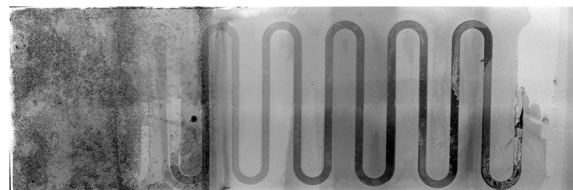


Fig. 11. Radiograph of sample D4 infiltrated by Si-8 at-pct Zr alloy at 1700 °C showed closure of the microchannel at 322 mm.

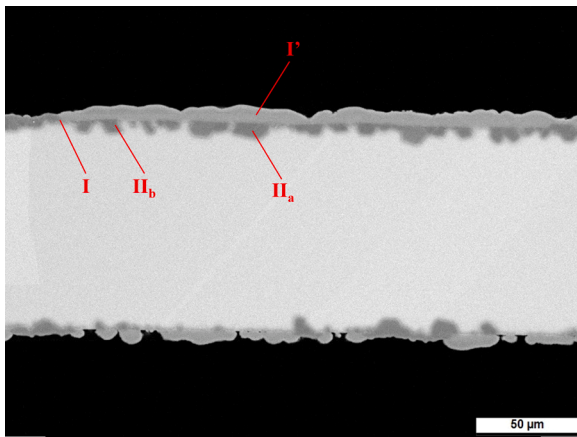


Fig. 12. BSE image of Si infiltrated 1 mm by 0.1 mm microchannel sample of configuration – A taken at 15 mm from bottom.

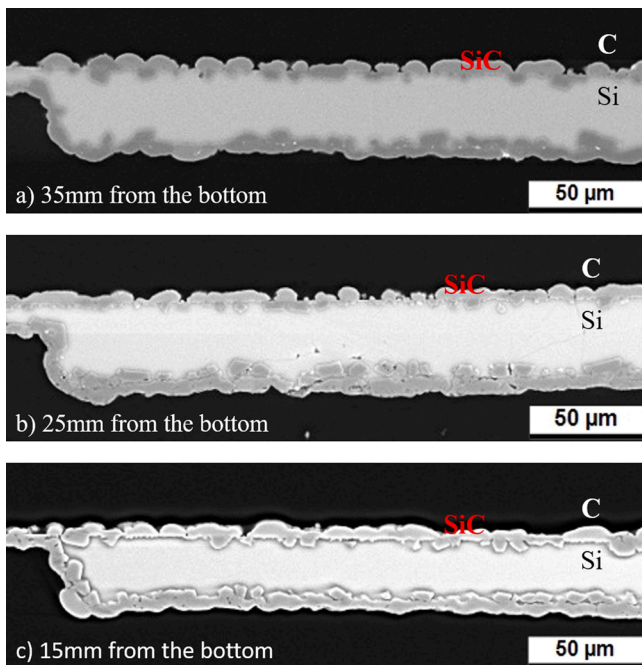


Fig. 13. SEM analysis of the reacted interface between silicon and vitreous carbon at 1500 °C, 1 mm × 0.025 mm microchannel sample of configuration A.

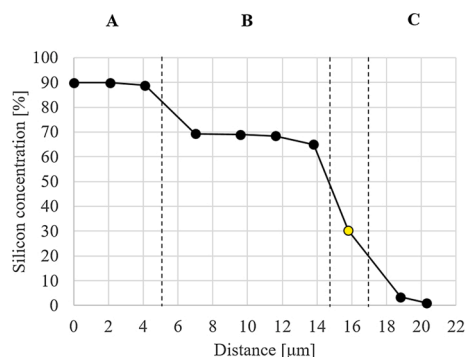


Fig. 14. Silicon concentration profile across the reaction zone formed between silicon and vitreous carbon.

seen in Fig. 14. The zones A, B and C in the Fig. 14 represent Si, SiC and vitreous carbon, respectively. The point in region C with a yellow marker shows a higher silicon concentration than expected. This was attributed to the larger spot size of the electron beam generating a signal from both SiC and C simultaneously at the interface. The silicon concentration drops from region A to B by approximately 22%, which gives the concentration ratio of $\text{Si}_A^B \approx 0.75$ which is in good agreement with the results from Voytovych et al. [37] and Deike et al. [47]. The concentration of silicon over zone B is nearly constant. The results show that the homogenization of the reaction zone occurs for long-term experiments, which leads to the depletion of layer I.

The mechanism of reaction formation of SiC layer at the interface of liquid Si and vitreous carbon was observed to be similar as in our previous studies [34] and the description of Voytovych et al. [37]. The formation of reaction layer between liquid Si and vitreous carbon occurs in three stages:

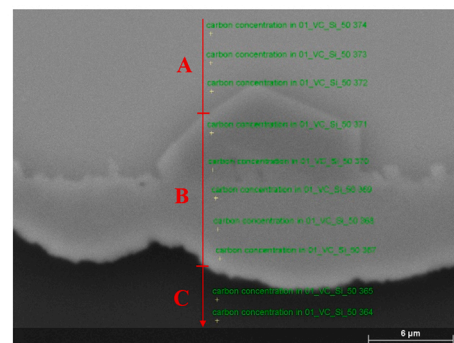
- at short times $t < 1$ min, nucleation and growth processes lead to the formation of an equiaxed, micron-thick layer of SiC;
- at intermediate times $1 \text{ min} < t < t^* \approx 20$ min thickening of the SiC layer occurs up to approximately 10 μm ;
- at long times $t > t^* \approx 20$ min the growth rate of the SiC layer becomes negligible and, due to the homogenization, the layer previously observed as a complex one is replaced by a single SiC layer.

The reaction zone between vitreous carbon and silicon has a relatively small thickness. This illustrates the low diffusion coefficient of Si and C in SiC. According to Gern and Kochendorfer [48], the SiC layer is formed as soon as the first contact between C and molten Si occurs. Thus, further thickening of the layer is controlled by the diffusion of Si and C in SiC. Eveno et al. [12] and Hon et al. [13,49] showed that the diffusion of C in SiC is much faster than the diffusion of Si. They also showed that both Si and C are more prone to diffuse via grain boundaries rather than by bulk lattice diffusion.

According to the comprehensive study done by Voytovych et al. [37] on the kinetics of reaction layer growth, the growth of SiC at $t < t^*$ and $t > t^*$ occurs by two different mechanisms. At short times $t < t^*$, during the growth of SiC crystals at the liquid Si/C interface, micrometer-sized holes are formed between SiC crystals, which enable direct communication between the carbon substrate and the bulk liquid through layer I. The thickening of the reaction layer throughout these times occurs by liquid state diffusion. However, at long times $t > t^*$, the layer I becomes impervious for the liquid Si, thus further thickening occurs by grain boundary diffusion. The reaction layer's growth rate becomes negligibly small; therefore, only the homogenization of the reaction layer is observed.

3.4. Interpretation of pore closure in Si vs Si-Zr alloy infiltration

Several researchers have proposed the pore occlusion model in LSI



with the help of classical sessile drop experiments [34,37,39], infiltration of C-C preform [35,43], infiltration of millimetre and sub-millimetre sized graphite capillaries [32,40,50]. Fundamentally, they all agree on the role of the solid-state reaction formed SiC in reducing the diameter of infiltration capillary. There are also studies involving and demonstrating use of silicide forming alloying elements to avoid pore closure by formation of solid SiC [20–27]. However, to the best of our knowledge, no consideration in the literature is given for the effect of the enrichment of the alloying element at the infiltration front as the Si in alloy reacts with the C from the capillary channel to form SiC.

For the sake of convenience, if we ignore the influence of the thickness of the reaction formed SiC layer in the inner wall of the tube, the infiltration length (L), reached by the alloy in the rectangular capillary channel with the thickness (e), in this case, the separation of the two glassy carbon plates due to the laser ablated groove, as derived in our previous work [51], can be written as follows:

$$L = \left[\frac{(c_{Si,0} - c_{Si}^{crit}) V_m^{SiC} e D_{diff,0}^{\frac{n-1}{2n}}}{(1 - c_{Si,0}) V_m^{liquid} 2 v_0^{\frac{n-3}{2n}} \theta_{SiC,0}} \exp \left[\frac{2nQ_{SiC} - (n-1)Q_{diff} - (3-n)Q_{triple}}{2nRT} \right] \right]^{\frac{2n}{n+1}} \quad (2)$$

where $c_{Si,0}$ is the initial concentration of Si in the alloy, c_{Si}^{crit} is the critical concentration of Si below which the precipitation of solid silicide phase occurs as per phase diagram at the given temperature, V_m^{SiC} is the molar volume of the SiC, V_m^{liquid} is the molar volume of the liquid alloy, $D_{diff,0}$ is the diffusion coefficient for Si in liquid Si-Zr alloy, v_0 is the prefactor for the triple line velocity at the given temperature, $\theta_{SiC,0}$ is the prefactor for the growth of SiC layer with time, R is the universal gas constant, T is the processing temperature, n is the parameter defining the order of growth kinetics and Q_{SiC} , Q_{diff} , and Q_{triple} are the activation energies for SiC formation, diffusion of Si in the alloy and triple line, respectively. The typical values for various parameters from the literature [9,52–54] are mentioned below:

$$\begin{aligned} V_m^{SiC} &= 1.25 \times 10^{-5} \text{ m}^3/\text{mol} \\ V_m^{liquid} &= 1.31 \times 10^{-5} \text{ m}^3/\text{mol} \\ D_{diff,0} &= 15 \times 10^{-9} \text{ m}^2/\text{s} \\ v_0 &= 2 \times 10^{-4} \text{ m/s at } 1500^\circ\text{C} \\ \theta_{SiC,0} &= 9 \times 10^{-6} \text{ m} \\ Q_{SiC} &= 200 \times 10^3 \text{ J/mol} \\ Q_{diff} &= 28 \times 10^3 \text{ J/mol} \\ Q_{triple} &= 185 \times 10^3 \text{ J/mol} \end{aligned}$$

The triple line velocity indicated here is significantly larger, by a factor of 5, roughly, than the observed triple line velocities in sessile drop spreading experiments. While the latter could be considered a good approximative indicator for the spreading rate on the microchannel's inner surfaces, the observed infiltration distances in pure Si experiments set a lower limit to triple line velocity. It is roughly this lower limit that has been chosen here. On the other hand, the thermal activation energy of the triple line velocity, Q_{triple} , is derived from observed spreading rates in sessile drop experiments at different temperatures [53].

The value of c_{Si}^{crit} in case of Si-Zr changes at peritectic temperature (1620 °C), below the peritectic temperature an approximate value of 0.72 is used while above the peritectic temperature 0.56 is used for the calculation; which was calculated by using the lever rule for a composition containing 80% solid phase fraction at a given temperature. Using the parameters mentioned above and Eq. (2), we can calculate infiltration length L with a varying initial concentration of Si, $c_{Si,0}$, for the values of $e = 10 \mu\text{m}$ and $e = 15 \mu\text{m}$ as shown in Fig. 15.

Due to the assumption to neglect the effect of channel closure due to the reaction formed SiC, the infiltration length values are unrealistic when the initial concentration of Si is close to 1 or $c_{Zr,0} \approx 0$.

Similarly, in Fig. 16, the effect of the temperature on the infiltration

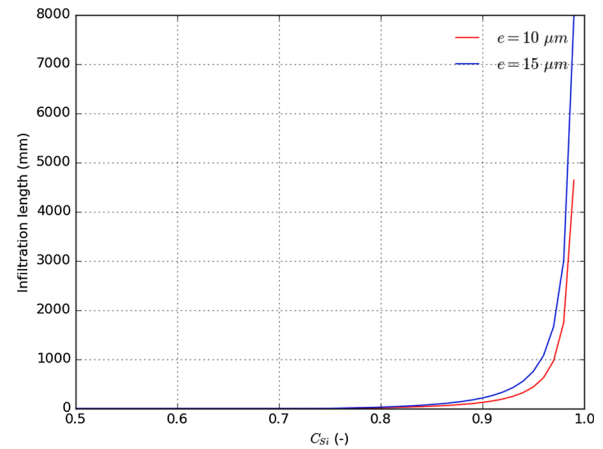


Fig. 15. Infiltration length as a function of the initial concentration of Si in the alloy for microchannels with depth $e = 10 \mu\text{m}$ and $e = 15 \mu\text{m}$.

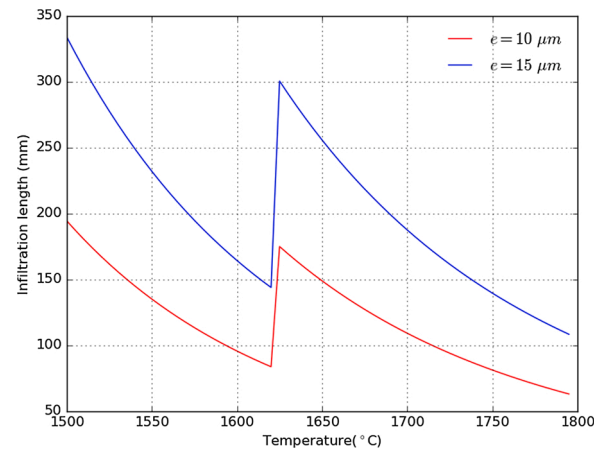


Fig. 16. The infiltration length achieved with increasing temperature for the microchannel depth $e = 10 \mu\text{m}$ and $e = 15 \mu\text{m}$ infiltrated with an Si-Zr alloy with an initial atomic concentration of Si $c_{Si,0} = 0.92$.

length is plotted for an initial atomic concentration of Si $c_{Si,0} = 0.92$ for the microchannel depth $e = 10 \mu\text{m}$ and $e = 15 \mu\text{m}$.

In our experiment of pure Si infiltration with 0.01 mm (e) channel (sample D3), we observed a complete infiltration of the channel of 465 mm length (Fig. 10). In the SEM image of a cross section of the channel at 5 mm from the exit end of the channel, we can see that the actual value of e is around 0.015 mm, mostly due to geometrical misfit

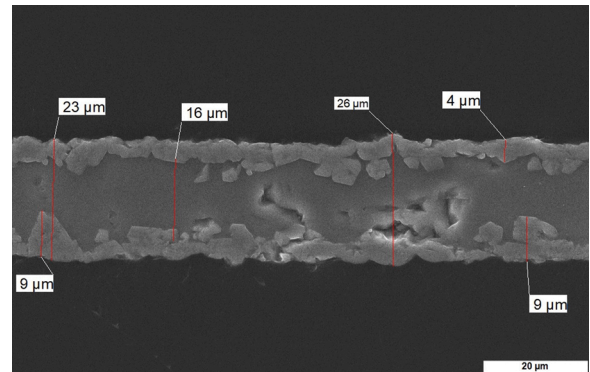


Fig. 17. SEM image of cross section taken at 5 mm from the exit end of 0.01 mm deep microchannel infiltrated with pure Si.

during the clamping of two plates and the cross section might not be at perfectly perpendicular plane (Fig. 17). The average SiC reaction layer thickness is around 5 μm . From this, we can conclude that the infiltration velocity for 0.01 mm capillary is fast enough to avoid the pore closure phenomenon for an infiltration distance of around 460 mm. However, much slower infiltration rates are observed during the infiltration of actual preforms due to higher tortuosity and non-uniform pores along the infiltration path [55]. Therefore, to observe the pore closure effect for infiltration by pure Si, a much lower microchannel depth is needed for the length of capillaries used in this study.

In the case of infiltration of sample D1 and D2 by Si-8 at-pct Zr alloy at 1500 °C, termination of the capillary rise was observed at approximately 166 mm and 120 mm, respectively. The variation in infiltration length might result from slightly different resulting depths due to the geometrical misfit of glassy carbon plates' straightness. This can also be seen in the calculated infiltration lengths for $e = 10 \mu\text{m}$ and $e = 15 \mu\text{m}$ in Figs. 15 and 16, where the infiltration length is longer for a higher value of e . However, the mechanism of obstruction is far different from that of pure Si. As the infiltration front moves along the capillary channel, the reaction of Si from the alloy with C forms SiC. The diffusive flux of Si is not high enough to compensate for the loss of Si due to reaction, enriching the Zr content of the liquid volume gradually at the front. This shifts the equilibria to the right side in the phase diagram as shown by the solid arrow in Fig. 18, where the temperature of infiltration is well below the solidus line to precipitate the zirconium silicides at the infiltration front. The reduced permeability due to further precipitation of zirconium silicides blocks the flow of liquid alloy, resulting in capillary choke-off. In the BSE images of the cross section of the sample D1 taken near the channel entrance, the SiC reaction layer can be observed at the entrance, while in the middle, solidified Si and ZrSi₂ can be seen. However, at the clogging location, the channel can be observed to be filled with zirconium silicides without any Si, which indicates the blockage of the channel is caused by the precipitation of ZrSi₂ and not only due to the formation of the SiC layer (Fig. 19) at the entrance. The topmost portion of the clogged channel from sample D2 showed SiC at the reaction interface on the C microchannel channel's inner walls and ZrSi₂ in the middle, as seen in Fig. 20.

By increasing the infiltration temperature to 1700 °C, a higher infiltration length of 322 mm was observed in sample D4 (Fig. 11). When we compare this to the calculated infiltration length value in Fig. 16 for 1500 and 1700 °C, we see that one should get a lower infiltration length for a higher infiltration temperature in the isothermal analysis. This discrepancy can be attributed to two things. First, the experiments'

setup does not allow controlling when the liquid should be in contact with the entrance of the microchannel. The infiltration starts as soon as the alloy is molten, somewhere around 1400 °C [34]. As the temperature continues to increase, near the peritectic temperature of the alloy, 1620 °C, there is a sudden increase in the infiltration length, and then again, it decreases with temperature. Since the furnace temperature increases as the infiltration front is progressing, the sudden decrease in solid volume fraction at the front can result in an overall increase in the infiltration length achieved. Numerical calculations using the non-isothermal model derived in our previous work [51] further highlight that the intermittent choke-off by Zr-enrichment is reached before reaching the maximum infiltration temperature. Therefore the triple line advances thanks to continuous alleviation of the choke-off concentration by diffusion. With the higher maximum temperature this diffusion mediated regime continues for a longer time and hence results in higher infiltration depth. A second factor that may have attributed to the observed higher infiltration length is a slight difference in value of e with increasing temperature, due the change in the gap between the glassy carbon plates held together by graphite fittings having different coefficient of thermal expansion. The EDX analysis of the top portion of the microchannel where clogging was observed, showed that the channel has ZrSi₂ and ZrSi in the centre of the channel and SiC at the inner walls, as seen in Fig. 21. It was also observed that some of the ZrSi₂ penetrated through the reaction layer to form tiny island like structures near the junction of two big SiC grains of the reaction layer. From the EDX analysis, it is evident that at 1700 °C, as the Zr concentration increases, the alloy composition shifts towards the right in the phase diagram, as shown by the dotted arrow in Fig. 18. At 1700 °C, the volume fraction of the solid primary phase decreases much more slowly and also sets in at higher Zr-concentrations.

4. Conclusion

With the innovative approach of laser ablated microchannels made from glassy carbon plates, the microscopic effects accompanying reactive melt infiltration can be observed experimentally. The extent of infiltration in the microchannels can be observed non-destructively using radiography. Both Si and Si-Zr alloy formed SiC at the inner walls of C microchannels. Two distinct mechanisms for pore-blocking were proposed in reactive melt infiltration of C for pure Si and Si-Zr alloy. In the case of the flow of pure Si in the microchannel, the microchannel's dimensions and tortuosity were not sufficiently small and sufficiently developed, respectively, to observe the blockage by the rapid formation of SiC at the ingress point experimentally. The infiltration velocity of Si in C is found to be too high compared to the rate of growth of the reaction layer, even for 0.01 mm deep microchannel to observe this phenomenon.

Another pore blockage mechanism was observed when it comes to infiltration by Si-Zr alloy in glassy carbon microchannels. As the alloy is rising in the capillary, Zr concentration increases gradually at the infiltration front due to the reaction of Si with C to form SiC. The enrichment of Zr in alloy volume results in the potential precipitation of zirconium silicides. The reduced permeability due to precipitated solid zirconium silicides further slows down the liquid alloy flow and finally blocks the capillary. The effect of an increase in infiltration temperature will depend on whether the experiment is conducted isothermally or in a gradual heating regime. In the isothermal case the more rapid formation of SiC is likely to actually reduce the ingress length despite the higher solubility of Zr in the liquid. In a gradually heating regime, the infiltration length may be expected to be larger the higher the final temperature is, in particular if the experiments are conducted above the peritectic temperature of ZrSi₂ formation. The sudden decrease in solid fraction above the peritectic temperature for the atomic concentrations of Zr above 0.33, leads to significantly longer infiltration length for both the isothermal and gradually heating process regimes. It is also in that temperature range, i.e., above the peritectic temperature, in which the

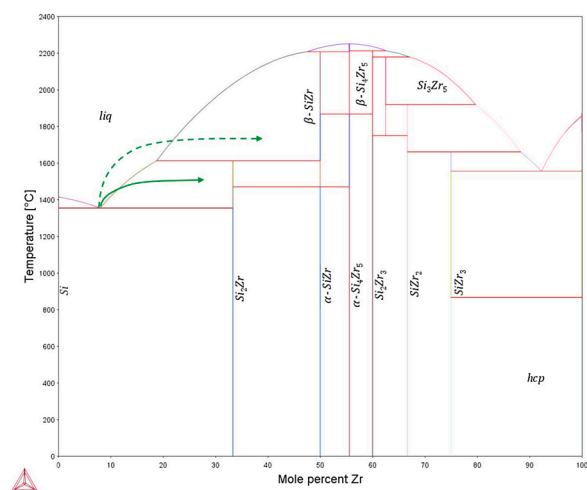


Fig. 18. Si–Zr phase diagram reproduced in Thermocalc using data from [56] showing the alloy composition shift as the alloy flows through microchannel at 1500 °C by a solid arrow and at 1700 °C by a dotted arrow.

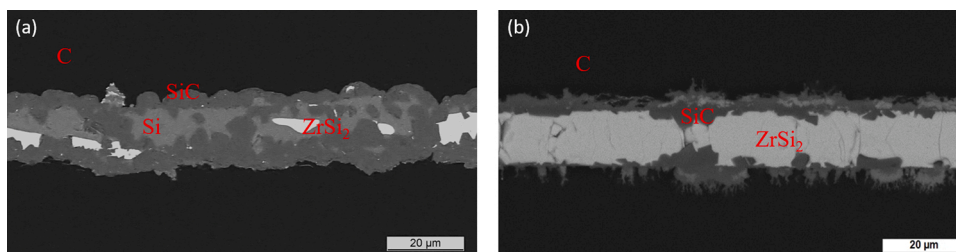


Fig. 19. BSE image of the cross section of sample D1, infiltrated at 1500 °C: (a) the region near the inlet of the microchannel showing SiC reaction layer and in the middle Si and ZrSi₂; (b) the clogging region showing SiC at the interface and solidified ZrSi₂ in the channel.

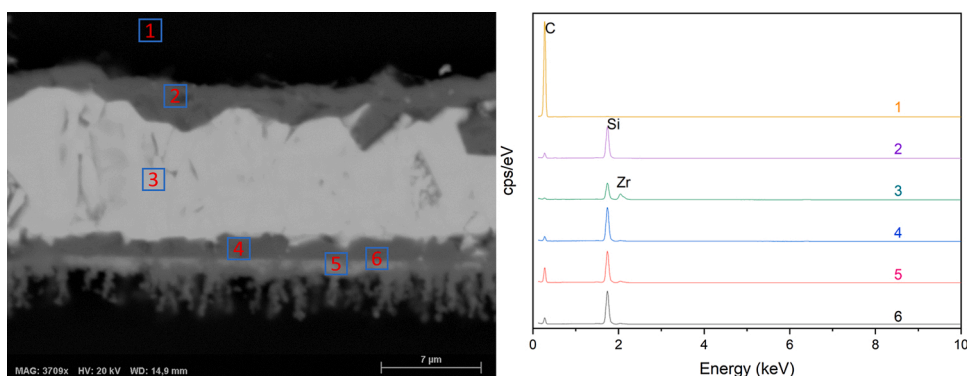


Fig. 20. BSE image of the cross section of sample D2, infiltrated at 1500 °C at the end of clogging region with EDX analysis at various points with different contrast.

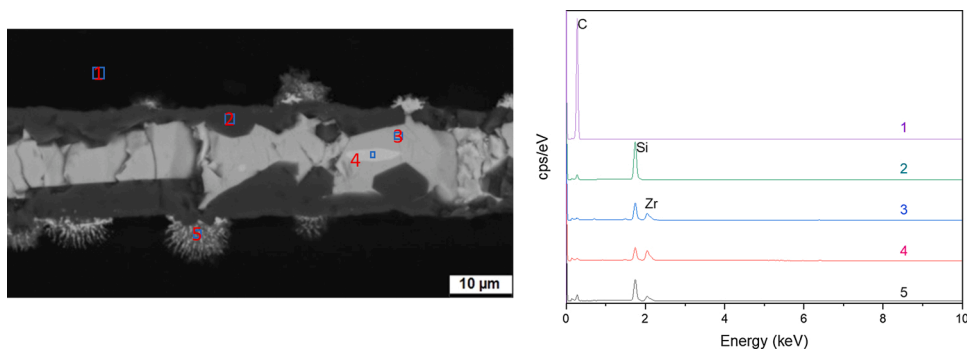


Fig. 21. BSE image of the cross section of sample D4, infiltrated at 1700 °C at the end of clogging region with EDX analysis at various points with different contrast.

both ZrSi₂ and ZrSi precipitate eventually leading to higher operating temperature than with free silicon. The ability to obtain high-temperature silicides by transient liquid-phase infiltration Si-Zr alloy into porous C makes it a suitable candidate to manufacture SiC composites, which can be used at higher operating temperatures than the melting point of pure Si. The phenomena described here are not limited to LSI with Si-Zr alloys but should, *mutatis mutandis*, also be transferable to LSI with other alloying systems.

Conflict of interest

None declared.

Declaration of Competing Interest

The authors report no declarations of interest.

Acknowledgements

The authors are grateful to Swiss National Science Foundation

(SNSF) for funding the project (Grant number 200021_163017). We would like to specially acknowledge the support of the Centre for X-ray Analytics, Empa, Swiss Federal Laboratories for Materials Science and Technology. We are grateful for the JECs Trust for funding the visit of Manoj Naikade to participate in the January 2019 ACerS Winter Workshop and conference to present his results in a poster presentation (Contract No. 2016124-29).

References

- [1] P. POPPER, *Special ceramics*, Soil Science 98 (2) (1964) 142. https://journals.lww.com/soilsci/Fulltext/1964/08000/Special_Ceramics.15.aspx.
- [2] N.P. Bansal, *Handbook of Ceramic Composites*, Springer US, 2006.
- [3] W. Krenkel, *Cost Effective Processing of CMC Composites by Melt Infiltration (LSI-Process)*, Ceramic Engineering and Science Proceedings, John Wiley & Sons, Inc, 2001, pp. 443–454, <https://doi.org/10.1002/9780470294680.ch52>. Book Section 52.
- [4] W. Krenkel, F. Berndt, C/C-SiC composites for space applications and advanced friction systems, *Mater. Sci. Eng. A Struct. Mater. Propert. Microstruct. Process.* 412 (1–2) (2005) 177–181, <https://doi.org/10.1016/j.msea.2005.08.204>.
- [5] W. Krenkel, B. Heidenreich, R. Renz, C/C-SiC composites for advanced friction systems, *Adv. Eng. Mater.* 4 (7) (2002) 427–436, [https://doi.org/10.1002/1527-2648\(20020717\)4:7<427::AID-ADEM427>3.0.CO;2-C](https://doi.org/10.1002/1527-2648(20020717)4:7<427::AID-ADEM427>3.0.CO;2-C).

- [6] A. Ortona, D. Trimis, V. Uhlig, R. Eder, S. Gianella, P. Fino, G. D'Amico, E. Boulet, C. Chazelas, T. Grämer, E. Cresci, J.G. Wünnig, H. Altena, F. Benek, M. Debier, SiC heat exchangers for recuperative gas burners with highly structured surface elements, *Int. J. Appl. Ceram. Technol.* 11 (5) (2013) 927–937, <https://doi.org/10.1111/ijac.12087>.
- [7] Y. Zhang, S. Li, J. Han, Y. Zhou, Fabrication and characterization of random chopped fiber reinforced reaction bonded silicon carbide composite, *Ceram. Int.* 38 (2) (2012) 1261–1266, <https://doi.org/10.1016/j.ceramint.2011.08.058>.
- [8] M.W. Chase, NIST-JANAF Thermochemical Tables Fourth Edition (Journal of Physical and Chemical Reference Data), American Institute of Physics for the National Institute of Standards and Technology, 1998.
- [9] O. Dezellus, S. Jacques, F. Hodaj, N. Eustathopoulos, Wetting and infiltration of carbon by liquid silicon, *J. Mater. Sci.* 40 (9–10) (2005) 2307–2311, <https://doi.org/10.1007/s10853-005-1950-7>.
- [10] R. Pampuch, E. Walasek, J. Białoskórski, Reaction mechanism in carbon-liquid silicon systems at elevated temperatures, *Ceram. Int.* 12 (2) (1986) 99–106, [https://doi.org/10.1016/0272-8842\(86\)90023-4](https://doi.org/10.1016/0272-8842(86)90023-4).
- [11] P. Sangsuwan, J.A. Orejas, J.E. Gatica, S.N. Tewari, M. Singh, Reaction-bonded silicon carbide by reactive infiltration, *Ind. Eng. Chem. Res.* 40 (23) (2001) 5191–5198, <https://doi.org/10.1021/ie001029e>.
- [12] P. Eveno, J. Li, A.M. Huntz, J. Chaumont, Diffusion of C-13 and Si-29 implanted ions in SiC, *Mater. Sci. Eng. B Solid State Mater. Adv. Technol.* 11 (1–4) (1992) 331–336, [https://doi.org/10.1016/0921-5107\(92\)90235-2](https://doi.org/10.1016/0921-5107(92)90235-2).
- [13] M.H. Hon, R.F. Davis, Self-diffusion of ^{14}C in polycrystalline β -SiC, *J. Mater. Sci.* 14 (10) (1979) 2411–2421, <https://doi.org/10.1007/bf00737031>.
- [14] J.F. White, L. Ma, K. Forwald, D. Sichen, Reactions between silicon and graphite substrates at high temperature: in situ observations, *Metall. Mater. Trans. B* 45 (1) (2013) 150–160, <https://doi.org/10.1007/s11663-013-9947-0>.
- [15] B.L. Wing, F. Esmonde-White, J.W. Halloran, Microstress in reaction-bonded SiC from crystallization expansion of silicon, *J. Am. Ceram. Soc.* 99 (11) (2016) 3705–3711, <https://doi.org/10.1111/jace.14398>.
- [16] V. Bougiouri, R. Voytovych, N. Rojo-Calderon, J. Narciso, N. Eustathopoulos, The role of the chemical reaction in the infiltration of porous carbon by NiSi alloys, *Scr. Mater.* 54 (11) (2006) 1875–1878, <https://doi.org/10.1016/j.scriptamat.2006.02.015>.
- [17] Y.M. Chiang, R.P. Messner, Method of preparing refractory silicon carbide composites and coatings, Patent number US5079195A (1992).
- [18] R.P. Messner, Y.-M. Chiang, Liquid-phase reaction-bonding of silicon carbide using alloyed silicon-molybdenum melts, *J. Am. Ceram. Soc.* 73 (5) (1990) 1193–1200, <https://doi.org/10.1111/j.1151-2916.1990.tb05179.x>.
- [19] R. Voytovych, V. Bougiouri, N.R. Calderon, J. Narciso, N. Eustathopoulos, Reactive infiltration of porous graphite by ni alloys, *Acta Mater.* 56 (10) (2008) 2237–2246, <https://doi.org/10.1016/j.actamat.2008.01.011>.
- [20] T. Aoki, T. Ogasawara, Y. Okubo, K. Yoshida, T. Yano, Fabrication and properties of Si-Hf alloy melt-infiltrated tyranno ZMI fiber/SiC-based matrix composites, *Compos. Part A: Appl. Sci. Manuf.* 66 (2014) 155–162, <https://doi.org/10.1016/j.compositesa.2014.07.009>.
- [21] S. Meier, J.G. Heinrich, Processing-microstructure-properties relationships of MoSi_2 -SiC composites, *J. Eur. Ceram. Soc.* 22 (13) (2002) 2357–2363, [https://doi.org/10.1016/S0955-2219\(02\)00035-3](https://doi.org/10.1016/S0955-2219(02)00035-3).
- [22] M. Singh, D.R. Behrendt, Reactive melt infiltration of silicon-molybdenum alloys into microporous carbon preforms, *Mater. Sci. Eng. A Struct. Mater. Propert. Microstruct. Process.* 194 (2) (1995) 193–200, [https://doi.org/10.1016/0921-5093\(94\)09663-5](https://doi.org/10.1016/0921-5093(94)09663-5).
- [23] Y. Tong, Z. Cai, S. Bai, Y. Hu, M. Hua, W. Xie, Y. Ye, Y. Li, Microstructures and properties of Si-Zr alloy based CMCs reinforced by various porous C/C preforms, *Ceram. Int.* 44 (14) (2018) 16577–16582, <https://doi.org/10.1016/j.ceramint.2018.06.081>.
- [24] T. Tsunoura, K. Yoshida, T. Yano, T. Aoki, T. Ogasawara, Fabrication and bending behavior of amorphous SiC-fiber-reinforced Si-Co eutectic alloy composites at elevated temperatures, *Compos. Part B: Eng.* 164 (2019) 769–777, <https://doi.org/10.1016/j.compositesb.2019.01.103>.
- [25] T. Tsunoura, Y. Okubo, K. Yoshida, T. Yano, T. Aoki, T. Ogasawara, Oxidation behavior of monolithic HfSi_2 and SiC fiber-reinforced composites fabricated by melt infiltration using Si-8.5 at% Hf alloy at 800–1200°C in dry air, *J. Ceram. Soc. Jpn.* 126 (1) (2018) 27–33, <https://doi.org/10.2109/jcersj2.17136>.
- [26] M. Caccia, S. Amore, D. Giuranno, R. Novakovic, E. Ricci, J. Narciso, Towards optimization of SiC/CoSi₂ composite material manufacture via reactive infiltration: wetting study of Si-Co alloys on carbon materials, *J. Eur. Ceram. Soc.* 35 (15) (2015) 4099–4106, <https://doi.org/10.1016/j.jeurceramsoc.2015.07.016>.
- [27] F.J. Narciso-Romero, A. Sepúlveda-Escribano, F. Rodríguez-Reinoso, A new route for the synthesis of SiC-MoSi₂ ceramic composite materials, *Chem. Commun.* (14) (1996) 1667–1668, <https://doi.org/10.1039/CC960001667>.
- [28] N.R. Calderon, R. Voytovych, J. Narciso, N. Eustathopoulos, Wetting dynamics versus interfacial reactivity of AlSi alloys on carbon, *J. Mater. Sci.* 45 (8) (2009) 2150–2156, <https://doi.org/10.1007/s10853-009-3909-6>.
- [29] N.R. Calderon, R. Voytovych, J. Narciso, N. Eustathopoulos, Pressureless infiltration versus wetting in AlSi/graphite system, *J. Mater. Sci.* 45 (16) (2010) 4345–4350, <https://doi.org/10.1007/s10853-010-4358-y>.
- [30] A. Ciftja, T.A. Engh, M. Tangstad, Wetting properties of molten silicon with graphite materials, *Metall. Mater. Trans. A* 41 (12) (2010) 3183–3195, <https://doi.org/10.1007/s11661-010-0362-8>.
- [31] B. Drevet, N. Eustathopoulos, Wetting of ceramics by molten silicon and silicon alloys: a review, *J. Mater. Sci.* 47 (24) (2012) 8247–8260, <https://doi.org/10.1007/s10853-012-6663-0>.
- [32] R. Israel, R. Voytovych, P. Protzenko, B. Drevet, D. Camel, N. Eustathopoulos, Capillary interactions between molten silicon and porous graphite, *J. Mater. Sci.* 45 (8) (2009) 2210–2217, <https://doi.org/10.1007/s10853-009-3889-6>.
- [33] J.-G. Li, H. Hausner, Wetting and infiltration of graphite materials by molten silicon, *Scr. Metall. Mater.* 32 (3) (1995) 377–382, [https://doi.org/10.1016/S0956-716X\(99\)80068-5](https://doi.org/10.1016/S0956-716X(99)80068-5).
- [34] M. Naikade, B. Fankhanel, L. Weber, A. Ortona, M. Stelter, T. Graule, Studying the wettability of Si and eutectic Si-Zr alloy on carbon and silicon carbide by sessile drop experiments, *J. Eur. Ceram. Soc.* 39 (4) (2019) 735–742, <https://doi.org/10.1016/j.jeurceramsoc.2018.11.049>.
- [35] J. Roger, L. Guesnet, A. Marchais, Y.L. Petitcorps, SiC/Si composites elaboration by capillary infiltration of molten silicon, *J. Alloys Compd.* 747 (2018) 484–494, <https://doi.org/10.1016/j.jallcom.2018.03.024>.
- [36] J. Roger, A. Marchais, Y. Le Petitcorps, Examination of the interaction between liquid silicon and bulk silicon carbide, *J. Cryst. Growth* 426 (2015) 1–8, <https://doi.org/10.1016/j.jcrysgro.2015.05.013>.
- [37] R. Voytovych, R. Israel, N. Calderon, F. Hodaj, N. Eustathopoulos, Reactivity between liquid Si or Si alloys and graphite, *J. Eur. Ceram. Soc.* 32 (14) (2012) 3825–3835, <https://doi.org/10.1016/j.jeurceramsoc.2012.05.020>.
- [38] Z. Yuan, W.L. Huang, K. Mukai, Wettability and reactivity of molten silicon with various substrates, *Appl. Phys. A Mater. Sci. Process.* 78 (4) (2004) 617–622, <https://doi.org/10.1007/s00339-002-2001-8>.
- [39] N. Eustathopoulos, R. Israel, B. Drevet, D. Camel, Reactive infiltration by Si: infiltration versus wetting, *Scr. Mater.* 62 (12) (2010) 966–971, <https://doi.org/10.1016/j.scriptamat.2010.02.030>.
- [40] D. Sergi, A. Camarano, J.M. Molina, A. Ortona, J. Narciso, Surface growth for molten silicon infiltration into carbon millimeter-sized channels: lattice-boltzmann simulations, experiments and models, *Int. J. Mod. Phys. C* 27 (6) (2016), <https://doi.org/10.1142/S0129183116500625>.
- [41] M. Bahraini, J.M. Molina, M. Kida, L. Weber, J. Narciso, A. Mortensen, Measuring and tailoring capillary forces during liquid metal infiltration, *Curr. Opin. Solid State Mater. Sci.* 9 (4–5) (2005) 196–201, <https://doi.org/10.1016/j.cossms.2006.02.007>.
- [42] E.O. Einstet, Capillary infiltration rates into porous media with applications to Silcomp processing, *J. Am. Ceram. Soc.* 79 (2) (1996) 333–338, <https://doi.org/10.1111/j.1151-2916.1996.tb08125.x>.
- [43] S. Kumar, A. Kumar, R. Devi, A. Shukla, A.K. Gupta, Capillary infiltration studies of liquids into 3d-stitched C-C preforms part b: kinetics of silicon infiltration, *J. Eur. Ceram. Soc.* 29 (12) (2009) 2651–2657, <https://doi.org/10.1016/j.jeurceramsoc.2009.03.006>.
- [44] N. Eustathopoulos, M.G. Nicholas, B. Drevet, Wettability at High Temperatures, vol. 3, Elsevier, 1999.
- [45] Y. Yuan, T.R. Lee, Contact Angle and Wetting Properties Springer Series in Surface Sciences, Springer Berlin Heidelberg, Berlin, Heidelberg, 2013, pp. 3–34, https://doi.org/10.1007/978-3-642-34243-1_1. Book Section Chapter 1.
- [46] J. Schindelin, I. Arganda-Carreras, E. Frise, V. Kaynig, M. Longair, T. Pietzsch, S. Preibisch, C. Rueden, S. Saalfeld, B. Schmid, J.-Y. Tinevez, D.J. White, V. Hartenstein, K. Eliceiri, P. Tomancak, A. Cardona, Fiji: an open-source platform for biological-image analysis, *Nat. Methods* 9 (7) (2012) 676–682, <https://doi.org/10.1038/nmeth.2019>.
- [47] R. Deike, K. Schwerdtfeger, Reactions between liquid silicon and different refractory materials, *J. Electrochem. Soc.* 142 (2) (1995), <https://doi.org/10.1149/1.2044109>.
- [48] F.H. Gern, R. Kochendorfer, Liquid silicon infiltration: description of infiltration dynamics and silicon carbide formation, *Compos. Part A Appl. Sci. Manuf.* 28 (4) (1997) 355–364, [https://doi.org/10.1016/S1359-835X\(96\)00135-2](https://doi.org/10.1016/S1359-835X(96)00135-2).
- [49] M.H. Hon, R.F. Davis, D.E. Newbury, Self-diffusion of ^{30}Si in polycrystalline β -SiC, *J. Mater. Sci.* 15 (8) (1980) 2073–2080, <https://doi.org/10.1007/bf00550634>.
- [50] P.J. Hofbauer, E. Radlein, F. Raether, Fundamental mechanisms with reactive infiltration of silicon melt into carbon capillaries, *Adv. Eng. Mater.* 21 (8) (2019) 1900184, <https://doi.org/10.1002/adem.201900184>.
- [51] M. Naikade, A. Ortona, T. Graule, L. Weber, Liquid Metal Infiltration of Silicon Based Alloys Into Porous Carbonaceous Materials. Part I: Modelling of Channel Filling and Reaction Phase Formation, 2021. Unpublished.
- [52] A.I. Pommrich, A. Meyer, D. Holland-Moritz, T. Unruh, Nickel self-diffusion in silicon-rich Si-Ni melts, *Appl. Phys. Lett.* 92 (24) (2008) 241922, <https://doi.org/10.1063/1.2947592>. Artn 241922.
- [53] D. Giuranno, A. Polkowska, W. Polkowski, R. Novakovic, Wetting behavior and reactivity of liquid Si-10Zr alloy in contact with glassy carbon, *J. Alloys Compd.* 822 (2020) 153643, <https://doi.org/10.1016/j.jallcom.2020.153643>. ARTN 153643.
- [54] J. Qin, X. Li, J. Wang, S. Pan, The self-diffusion coefficients of liquid binary M-Si (M=Al, Fe, Mg and Au) alloy systems by first principles molecular dynamics simulation, *AIP Adv.* 9 (3) (2019) 035328, <https://doi.org/10.1063/1.5067295>.
- [55] F.A.L. Dullien, M.S. Elsayed, V.K. Batra, Rate of capillary rise in porous-media with nonuniform pores, *J. Colloid Interface Sci.* 60 (3) (1977) 497–506, [https://doi.org/10.1016/0021-9797\(77\)90314-9](https://doi.org/10.1016/0021-9797(77)90314-9).
- [56] H.M. Chen, F. Zheng, H.S. Liu, L.B. Liu, Z.P. Jin, Thermodynamic assessment of B-Zr and Si-Zr binary systems, *J. Alloys Compd.* 468 (1–2) (2009) 209–216, <https://doi.org/10.1016/j.jallcom.2008.01.001>.